

Bond Stripe Patterns in $SU(3)$ spin model on the checkerboard lattice

Jun-Hao Zhang,^{1,*} Jie Hou,¹ Jie Lou,^{1,†} and Yan Chen^{1,‡}

¹*Department of Physics and State Key Laboratory of Surface Physics, Fudan University, Shanghai 200433, China*
(Dated: October 23, 2024)

As a generalization of the $SU(2)$ Heisenberg model on the Kagomé lattice, we examine the $SU(3)$ spin model on the checkerboard lattice. Geometric frustration results from this model's inheritance of the point-connected $(N+1)$ -site local structure. The ground state of the system is obtained by numerical algorithms. When system sizes and boundary conditions are appropriate, it favors global bond stripe patterns. The direction and structure of the bond stripe patterns are sensitive to the system size and boundary conditions. Additionally, we computed many correlation functions. The 3-sublattice antiferromagnetic order and valence cluster solid order are suppressed. Their decay tendencies are faster than those of the square lattice model. The stripes are relatively decoupled and can be rebuilt in quasi-one-dimensional ladders. This indicates that the ground state is brought towards the spin-liquid phase and away from the valence cluster solid state via frustration.

I. INTRODUCTION

Over the past few decades, frustrated magnets have attracted significant attention from researchers. The physics of frustrated magnets is dominated by quantum fluctuations with the conventional magnet order suppressed. Various complex quantum effects, including quantum criticality, topological orders, and long-range entanglement, emerge in frustrated magnets. Exotic quantum phases such as quantum spin liquid have been discovered in frustrated spin systems. In the model studies, the frustrated magnets will exhibit rich properties depending on the source of frustration of the system and the characteristics of the system.

A type of intriguing systems are those with $SU(N)$ symmetry. Alkaline-earth-like atoms trapped in an optical lattice, such ^{179}Yb and ^{87}Sr , can be used to realize this symmetry [1–4]. They show no magnetic momentum from electrons due to its two outermost electrons. Instead, the interactions of the hyperfine structure can be manipulated finely by orbital Feshbach resonance [5–7] so that the systems hold $SU(N)$ symmetry [8, 9]. Different values of N and various optical lattice geometries are realized and investigated experimentally [10–14]. New techniques for ultracold two-dimensional Hubbard or Heisenberg type quantum simulations have been developed recently [15, 16].

These systems are often described as $SU(N)$ Fermi Hubbard models [17]. It is a natural generalization of the conventional Fermi Hubbard model, with hopping parameter t and on-site repulsion U . This model has been intensively studied in the last decades [18–21]. The case of $N = 3$ is especially of research concern due to its connection to gauge symmetry of quantum chromodynamics and its computational friendliness. Recent research on square lattice shows metal-insulator transition and quantum antiferromagnetic order of different periods near integer fillings [22, 23]. For one-dimensional systems, trion molecular superfluid order and topological phases are discovered [24, 25]. On the other hand, as the strong corre-

lated limit of the $SU(N)$ Fermi Hubbard model, the $SU(N)$ t - J model also has unique properties [26–28].

The spin model occurs at $1/N$ -filling ($\langle n \rangle = 1$) in large U limit for the $SU(N)$ Fermi Hubbard model [29]. At this point, charge fluctuations are suppressed by Mott physics and the interaction between spin degrees of freedom can be derived through second-order perturbation theory.

Numerous new physics were found in the study of $SU(N)$ spin models in two-dimensional systems [30, 31]. A general phase diagram of the $SU(N)$ Heisenberg model is obtained by large N approximation meanfield calculation [21, 29, 32, 33]. The phase diagram includes chiral spin liquid for large N , valence cluster solid for small N , and some stripe state with flux for medium N . The chiral spin liquid phase is also confirmed in the tensor network calculation of some $SU(N)$ spin model with chiral interaction [34–36]. For the case of $N = 3$ on square lattice, three-sublattice order is predicted by multiple methods [37–40]. On the other hand, there are also density matrix renormalization group (DMRG) results showing it to be a fragile nematic spin liquid [41–43]. Taking advantage of this non-abelian symmetry, many state-of-the-art numerical techniques are also developed for these systems and get results with incredible scale and precision [44, 45].

The local frustrated structure for the $SU(N)$ spin model differs from that of the $SU(2)$ case. The local frustration structure changes from a triangle to a tetrahedron for the $N = 3$ case. The checkerboard lattice discussed in this paper is not only a 2D combination of local frustrated structures sharing corners but also a kind of line graph lattice. The line graph lattice is the link-point duality of the original lattice, similar to Kagomé lattice. The tight-binding models on the line graph lattice have a high degree of degeneracy in the energy spectrum, which results in a flat energy band. This feature brings many intriguing physics, including nontrivial topology, band ferromagnetism, and superconductivity [46–51]. Experimentally, this lattice has been realized in monolayer Cu_2N [52]. The conventional spin model on checkerboard lattice has also received attention in theoretical research [53–61]. This lattice is also studied for the $SU(4)$ spin model as an appropriate system for 4-site simplex valence cluster solid (VCS) state [62].

In this paper, we study the ground state of the frustrated $SU(3)$ spin model on checkerboard lattice. Through exact

* jhzhang16@fudan.edu.cn

† loujie@fudan.edu.cn

‡ yanchen99@fudan.edu.cn;

diagonalization (ED) and DMRG calculations, we determine the ground state for a Hamiltonian tuned from square lattice to checkerboard lattice. By using both algorithms, we observe a quantum phase transition between the models. For ED results, the degeneracy of ground state changes, and the correlation becomes weaker in DMRG results. Additionally, we compare different low-energy states computed by DMRG and conclude from the results that a bond stripe pattern is favorable. Next, we study the nature of stripe states and find that the bond stripes are almost decoupled. We thus characterize the single-stripe subsystems and reproduce the stripe in quasi-one-dimensional ladders. Finally, we summarize our findings and discuss the relation to the previous works and some low-energy effective theory.

The organization of our paper is as follows. In Sec. II, we introduce the SU(3) Heisenberg model on checkerboard lattice and the parameter settings of the DMRG simulations. In Sec. III, we show our numerical results including the various correlations and different local quantities. In Sec. IV, we study the nature of stripe states and reproduce the stripe in quasi-one-dimensional ladders. The final section Sec. V is the summary and discussion.

II. MODEL

A. SU(3) symmetric Hamiltonian

The 2-site SU(3) symmetric spin Hamiltonian is constructed by taking $N = 3$ with general SU(N) Heisenberg exchange Hamiltonian

$$\mathcal{H}_{ij}^{\text{SU}(N)} = JP_{ij} = JS_i^{\alpha\beta} S_j^{\beta\alpha}, \quad (1)$$

where P_{ij} exchanges local state on 2 sites, and $S_i^{\alpha\beta} = c_{i\alpha}^\dagger c_{i\beta}$ are the SU(N) spin operators in terms of fermion operators. The summations of α and β go over the N flavors of spin. In the following, we will concentrate on the case with fundamental irrep described by the Young diagram \square . There are several good quantum numbers for this interaction. The total spin components $L^{3,8}$ together with 2nd Casimir C^2 are conserved. The numerical calculation can be accelerated by taking advantage of these good quantum numbers.

B. Checkerboard Lattice

The geometric frustration for ordinary spin systems is often illustrated by triangle structures [63, 64]. For models where a singlet requires two lattice sites to form, such as spin-1/2 systems, the model on the Kagomé lattice is considered to be frustrated. It is made up of triangles sharing only 1 corner with each of their neighbors. For SU(3) symmetry, singlet formation requires 3 fundamental irreps. Specifically, singlet would occupy 3 sites in Hamiltonian Eq. (1). Consequently, the local frustration structure should be generalized to connected 4 sites (FIG. 1). By repeating this structure in the way sharing only 1 corner with each of their neighbors, we can

get pyrochlore lattice in 3D. The checkerboard lattice is an alternative choice as the planar pyrochlore structure (FIG. 1). These lattices can be classified as line graphs of different original lattices with a flat upper energy band.

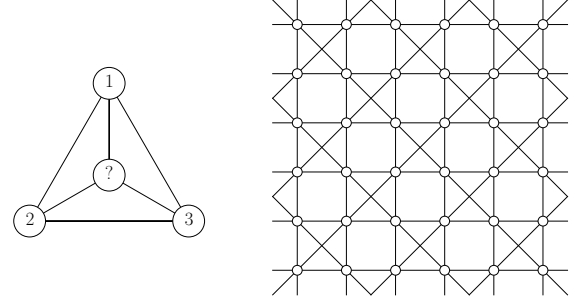


FIG. 1: Local frustration structure for SU(3) fundamental irreps (left panel) and checkerboard lattice (right panel).

To relate with the previous results for square lattice, checkerboard lattice is regarded as a square lattice with next-nearest-neighbor (NNN) interactions on half of the plaquette. The Hamiltonian could be written as

$$H_{\text{Checkerboard}}^{\text{SU}(N)} = \sum_{\langle i,j \rangle} JS_i^{\alpha\beta} S_j^{\beta\alpha} + \sum_{\langle\langle i,j \rangle\rangle} J_{\times} S_i^{\alpha\beta} S_j^{\beta\alpha}. \quad (2)$$

We can tune the system from square lattice to checkerboard lattice by taking J_{\times} from 0 to J . This would reveal whether the ground states on the square lattice are in the same phase as the ground states. With no loss of generality, we choose $J \equiv 1$ to set the overall energy scale. The size of unit cells in the checkerboard lattice is twice the ones in the underlying square lattice, which contains 2 sites. The base vector's direction is rotated $\pi/4$ with respect to the square lattice, and its length is $\sqrt{2}a$.

III. NUMERICAL RESULTS

We use ED and DMRG to study the ground state of this model. We employ the QuSpin package [65, 66] for ED computations. Periodic boundary conditions are applied for both directions in ED. Meanwhile, the DMRG simulations are performed with the help of the ITensor library [67]. A maximum bond dimension $D_{\text{max}} = 6000$ is kept in DMRG simulations. The calculation is typically performed for around 100 sweeps, and the largest truncation errors of final wave functions are about 10^{-5} . The global conservation of the SU(3) spin component is kept as good quantum numbers for saving computing resources.

A. ED Result

We calculate the energy spectrum of several lowest energy states for the system with size 3×3 unit cells, which contains

18 sites. The NNN interaction strength J_\times varies from 0 to 1 to show distinct phases. The spectrum is illustrated in Fig. 2. A phase transition is found near $J_\times = 0.45$, where energy levels intersect. The ground state is unique for $J_\times < 0.45$ and 2-fold degenerate for $J_\times > 0.45$.

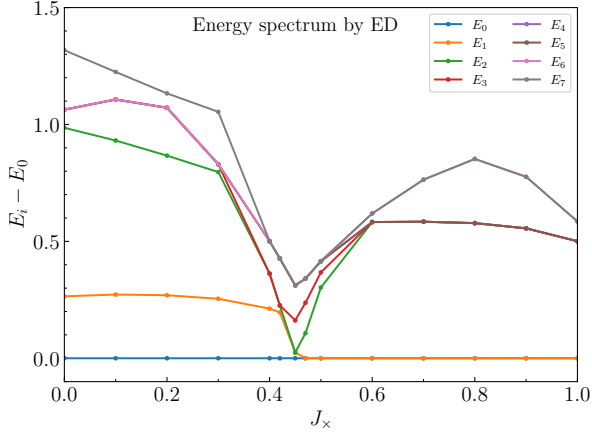


FIG. 2: Low energy spectrum of 3×3 system.

This 2-fold degeneracy could be split by breaking the lattice symmetry from c_4 to c_2 . Specifically, we can apply different J_\times in different directions to split 2-fold degenerate ground states. We obtain the coupling strength along interaction bonds. The 2 degenerate ground states show a slight difference in the NNN couplings along different directions. The local spin component n_i^α and coupling strength $B_{ij} = \hat{L}_i^3 \hat{L}_j^3$ is shown in Fig. 3. The NNN coupling strengths B_{NNN} along 2 directions have little difference in value as -0.104 and -0.093. As a result, the degenerate ground states are symmetry-breaking states, probably like nematic spin liquid [42]. Moreover, when J_\times becomes stronger than 1.15, the ground state becomes direct product of six singlets along the x, y directions. This is because the finite system size brings singlets that cross the boundary, which is not allowed in the thermodynamic limit.

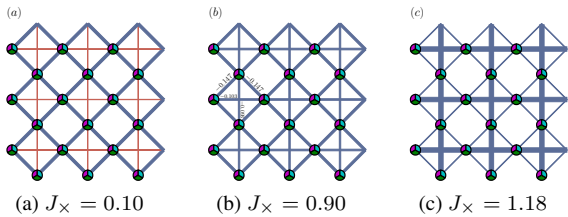


FIG. 3: Real-space coupling patterns of the ground states in two phases. (a) unique ground state when $J_\times = 0.10$; (b) one of two degenerate ground states when $J_\times = 0.90$; (c) unique ground state when $J_\times = 1.18$. The pie charts represent the local spin component on each site. The width of lines represents the strength of coupling. Its color takes blue and red for antiferromagnetic and ferromagnetic coupling.

B. DMRG Result

The ED result shows a phase transition between square and planar pyrochlore lattices. However, it introduces strong finite size effects and provides little information about correlations. Then we study the ground state with the DMRG algorithm for larger system sizes.

The DMRG calculations are performed on cylinders, with open boundary conditions in the x direction and periodic boundary conditions in the y direction. The system size is set as $N_x \times N_y$ unit cells, including $N_{\text{tot}} = 2N_x N_y + N_y$ sites. The extra N_y sites are boundary sites on one of the open boundaries. We compute multiple sizes, where N_x varying from 7 to 10, and N_y varying from 4 to 6. The size of the systems is chosen such that N_{tot} is a multiple of 3.

Corresponding to the results of ED, we study the evolution of the ground state as J_\times from 0 to 1. We measure the spin correlation function

$$S(r) = \langle \hat{L}_i^3 \hat{L}_{i+\vec{r}}^3 \rangle, \quad (3)$$

where $\hat{L}_i^3 = \hat{n}_i^{\alpha=1} - \hat{n}_i^{\alpha=2}$ is one of the Gell-Mann generator. Different behaviors are observed for weak and strong NNN interactions (Fig. 4a). It shows a shorter correlation length in the strong interaction case, significantly different from weak interaction cases. This indicates a phase transition between ground states on square and planar pyrochlore lattices.

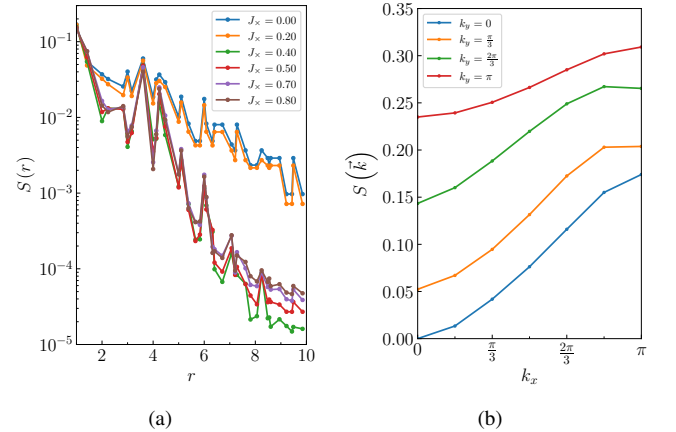


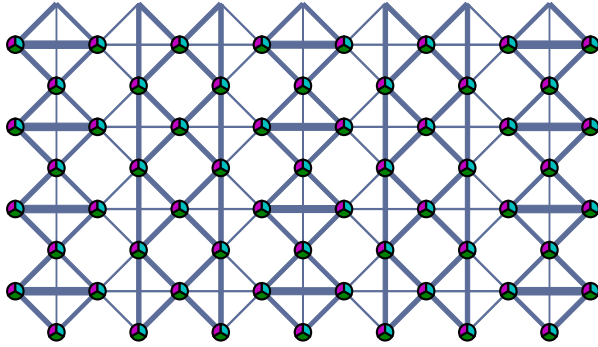
FIG. 4: Spin correlation (a) Spin correlation with different J_\times ; (b) Fourier transform of spin correlation.

The shorter spin correlation length indicates the break of 3-sublattice antiferromagnetic order. The fourier transformation of the spin correlation function is shown in Fig. 4b. Since it is smooth and exhibits underlying quadratic behaviors close to the origin, a finite spin gap and no spin order are most likely. We also study planar pyrochlore lattice systems in square lattice geometry (Details in Supplemental Materials). The spin correlation function along the side of the plaquette shows a short correlation length of $r_S = 0.91a$. We also try to induce 3-sublattice AF order and valence bond (or cluster) solid order by applying corresponding field on the boundary. The

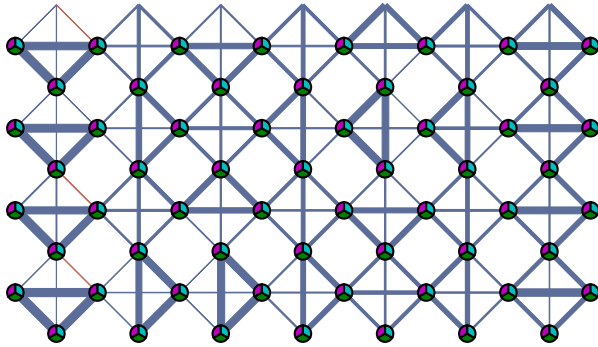
results don't support these orders. (Details in Supplemental Materials)

C. Real-Space Valence Bond Coupling

After confirming the absence of 3-sublattice antiferromagnetic order and simple triangular VCS order, we focus lattices on unit cell direction. The ground states exhibit some real space structure in a variety of system sizes. In the system size (7, 4) (no long singlet cross the boundary, 60 sites in total as multiple of 3), the local valence bond strength of the lowest energy state shows a stripe pattern (Fig. 5a). This stripe pattern has a period of 3 unit cell lengths in the x direction and doesn't break translational symmetry in the y direction. Sometimes the DMRG simulation would converge to another ground state structure. It has an apparent local triangle pattern in valence bond strength, but the triangles are not arranged in a clear periodicity as a VCS phase. The energy of this local minimum state is also a little higher than the stripe pattern state.



(a) (7, 4) Stripe Structure



(b) (7, 4) Local Minimum

FIG. 5: (5a) Ground state and (5b) local minimum state real-space bond strength obtained by DMRG simulation for the system size of (7, 4). The energy of the states are (5a) $E_0 = -201.698$, (5b) $E_1 = -201.468$.

We also calculate the ground state of larger system sizes, up to (10, 6) (Details in Supplemental Materials). There are lo-

cal minimum states for different system sizes. We summarize some of the lowest energy states for different sizes in Table I.

We discover several coupling laws for this model. The coupling structure near the system boundary has significant features. For the straight open boundaries longer than 5 unit cells, the coupling structure is arranged by repeated triangles, which breaks reflection symmetry along the boundary. For the 4 unit cell width case, the reflection symmetric boundary could be regarded as a superposition of triangle arrays with different orientations. The stronger coupling strength on the bond vertical to the boundary. These triangular singlets are connected into a boundary ring. Reflection transformation to this boundary ring would not change system energy.

For systems with length $3n + 1$ in x direction, the stripe phase with 3-unit-cell stripe has better energy. This stripe pattern consists of a one-unit-cell-width triangle array as the boundary pattern and a 2-unit-cell-width reflecting symmetric pattern. We call the strong coupling bond a flat stripe. The energy of the flat stripe is lower than the energy of two corresponding staggered triangle VCS patterns. By comparing local minimum states in the same size, we find the more stripe pattern, the better energy it has.

For systems with other lengths in x direction, the stripe phase can't fit the system well. When the length in y direction is 6, there is a clear triangle pattern. It shows a 2-unit-cell-width periodic triangle configuration away from the open boundary. As the length in x direction increases, this triangle configuration would make up a vertical stripe-like configuration. So we come to the domain law that the stripe pattern reduces the local energy, while the boundary pattern serves as a constraint to the global coupling structure.

For stripe phase, we calculate several correlation functions and show them in Fig. 6. It includes spin correlation function Eq. (3), chiral correlation function

$$\chi(r) = \langle \chi_{ijk} \chi_{i'j'k'} \rangle, \quad (4)$$

and nematic correlation function

$$\eta(r) = \langle \eta_x \eta_{x+r} \rangle - \langle \eta_x \rangle \langle \eta_{x+r} \rangle. \quad (5)$$

The local chiral and nematic operators are defined as $\chi_{ijk} = i(P_{ijk} - P_{ijk}^{-1})$ and $\eta_i = (B_i^x - B_i^y)$, where P_{ijk} rotates states on 3 sites and $B_i^{x,y}$ is bond coupling along the x, y in a unit cell. These correlation functions show exponential decay, with a short correlation range less than the length of the square side. This result excludes the possibility of these orders in the checkerboard lattice.

IV. BOND STRIPE PATTERN

Bond stripe patterns have been discovered in meanfield calculation for the $SU(N)$ Heisenberg model by the self-consistent minimization algorithm. They are low energy states for $N = 4, 5$ on triangle lattice and $N = 5, 6$ on square and J_1 - J_2 honeycomb lattice [32, 33, 68]. However, in stark contrast to the doubled unit-cell bond stripe state they find, the

Algorithm	Size	Number of Spins	Number of bonds	Valence Bond Coupling Structure	Energy	Energy per bond
ED	(3, 3)	18	54	Nematic(Fig. 3b)	-64.343	-1.1915
DMRG	(7, 4)	60	168	Triangle(Fig. 5b)	-201.468	-1.1992
				Stripe(Fig. 5a)	-201.698	-1.2006
	(10, 4)	84	240	Stripe	-286.548	-1.1940
				Triangle & Stripe	-286.283	-1.1928
	(7, 5)	75	210	Incompatible	-250.520	-1.1929
				Stripe	-250.928	-1.1949
	(7, 6)	90	252	Incompatible	-299.661	-1.1891
				Stripe	-300.598	-1.1928
	(8, 6)	102	288	Triangle	-342.361	-1.1887
				Incompatible	-384.193	-1.1858
	(9, 6)	114	324	Triangle	-384.070	-1.1854
				Triangle & Stripe	-384.550	-1.1868
	(10, 6)	126	360	Triangle	-426.819	-1.1856
				Stripe	-426.903	-1.1858

TABLE I: Energy of the ground state and local minimum states for different system sizes. Some of the real space bond strength structures are shown in supplemental materials.

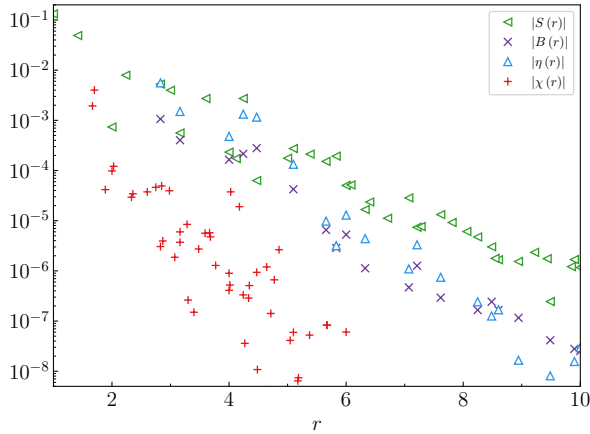


FIG. 6: Spin correlation $S(r)$, bond correlation $B(r)$, nematic correlation $\eta(r)$ and chiral correlation $\chi(r)$ measured in system with size $(N_x, N_y) = (10, 6)$. They all show exponential decay. The correlation lengths are $r_S = 0.89a$, $r_B = 0.55a$, $r_\eta = 0.61a$ and $r_\chi = 0.32a$, a is the length of square side.

stripe phase in this work is a tripled one. The stripe states they discover have $U(1)$ gauge flux, which is absent in this work. On the other hand, the ground states for $N = 3$ is the VCS state which consists of singlets with 3 or 6 sites in such mean-field calculations. While the validity of the large N approximation applied in the meanfield approach may not be well ensured. The J_\times interaction, according to our computation, suppresses the 3-sublattice order and global VCS order, resulting in a bond stripe phase that differs from the meanfield result.

The flat part of the stripe pattern would break translation symmetry into triangle VCS pattern when meeting the boundary triangle array or stripe corner. This implies the state is a direct product state. We calculate the entanglement entropy for the subsystems cutting on different lines in FIG. 7. The edge length dependence of entanglement entropy between the stripes is also calculated. The entanglement entropy for subsystems cutting weak bonds is lowest and approximately equal for different boundary lengths of subsystems. The periodicity of entanglement entropy further suggests that entanglement has a very limited range. The stripes are separated spin singlet on the occupied sites. This explains why the range of correlation across the stripes is necessarily short.

A. Decoupled Stripe and Single-Stripe Ladder

Since every stripe is almost pure, it is possible to compute the correlation in a stripe on the ladder stripe that it occupies. We use ED to reconstruct the single-stripe patterns in a system consisting of four to six unit cells.

We obtain results for triangle array that are comparable to the previous exact solution for the spin tetrahedron chain [56]. The ground state is of two-fold degeneracy that could be broken by violating the reflection symmetry. The symmetry-broken states have the same pattern as triangle arrays in stripe states. They are pure direct product states. The flat stripe is also reproduced in isolated ladder systems. The ground state is unique and has uniform coupling strength $B = -0.1986$ on each bond.

We further use the DMRG algorithm to study the more long-range correlation functions within the stripes. The real space pattern is shown in FIG. 8a. The result for the triangle array stripe ladder is consistent with the results of the ED

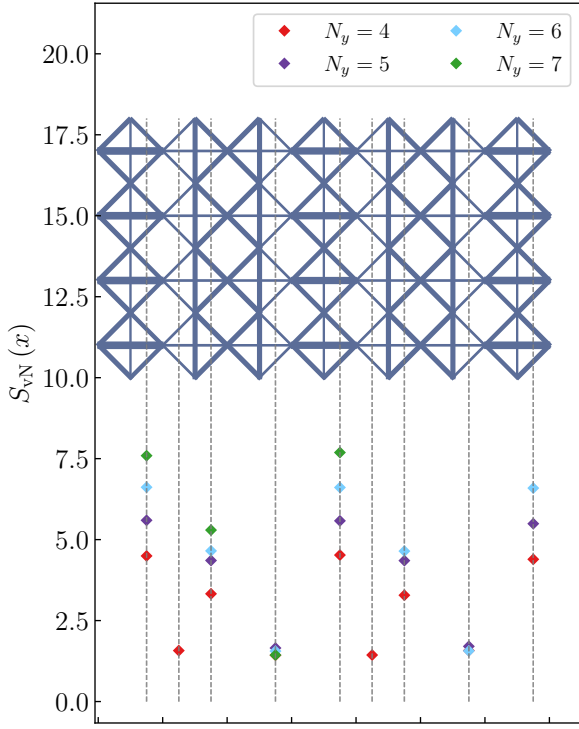


FIG. 7: Entanglement entropy for division at different position. The dashed lines mark the system division position and the red bars below represent the value of entanglement entropy at dashed line. It shows distinct periodicity, with approximate minima between stripes and maxima on cutting triangle arrays.

calculation as a direct product of triangle singlets, whose correlation functions match the VCS state.

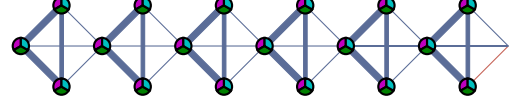
For the flat stripe ladder system, we compute the system length up to 64 unit cells, whose maximum kept dimension for truncation errors less than 10^{-10} is $D = 1467$. This limited bond dimensions suggests that this quasi-one-dimensional system is gapped. As is shown in FIG. 8b, there is no spontaneous breaking of translational symmetry and spatial inversion symmetry in the results of the DMRG calculations. When we examine the valence bond strengths away from the boundary, there is a difference between the valence bond strengths in the direction parallel to the chain direction and diagonal to the chain direction of $B_{\parallel} = -0.1848$ and $B_{\times} = -0.1993$, respectively. This is similar to results for the two-dimensional case in the ratio (~ 0.93) of the two kinds of bonds (e.g., $B_{\parallel}^{2d} = -0.175$ and $B_{\times}^{2d} = -0.1846$ in the (10, 6) system).

The correlation functions of the flat stripe ladder system also have highly similar behavior to the 2-dimensional case. The spin and bond correlation functions for the flat stripe ladder system are shown in FIG. 8c. They both show exponential decay with correlation lengths $r_S^{1d} = 1.73a$ and $r_B^{1d} = 2.82a$, respectively. We calculate the corresponding correlation func-

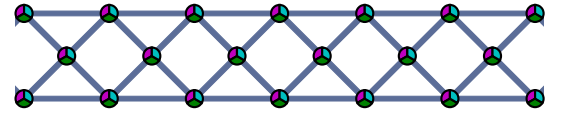
tion of 4-point chirality

$$\chi_{ijkl}^4 = \frac{i}{4} (P_{ijkl} - P_{ijkl}^{-1}), \quad (6)$$

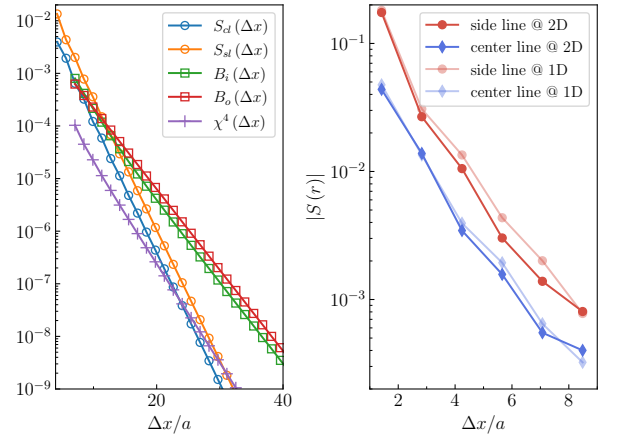
where i, j, k, l is defined on the square part. They also decay exponentially, failing to corroborate the gauge flux of the stripe state in mean-field calculations.



(a) Single triangle-array ladder.



(b) Flat stripe ladder.



(c) Correlation function in flat stripe ladder.

FIG. 8: (a), (b) the local spin and bond pattern of the triangle array ladder and the flat stripe ladder, respectively. (c) (left) Spin correlation along center line S_{cl} and side line S_{sl} . Bond correlation of inner bonds B_i and outer bonds B_o . (right) Comparison of spin correlation functions for flat stripes in 2D and 1D systems.

V. SUMMARY AND DISCUSSION

Singlet occupying 3 sites is frustrated on vertex-connected tetrahedrons, which form pyrochlore lattices. By using ED and DMRG simulations, we have studied the SU(3) spin model on the checkerboard lattice, so-called the planar pyrochlore. We observe the quantum phase transition between the square lattice model and the checkerboard lattice model by adjusting the diagonal couplings. The 3-sublattice antiferromagnetic order is suppressed when the diagonal couplings

are added to the model. The stripe pattern appears frequently in the DMRG calculations, and the stripe state serves as global ground state in suitable system sizes. The 2-fold degeneracy of the ground states in ED calculation is also consistent with the c_4 symmetry breaking of the stripe phase. The stripes are rather decoupled, leading to short-range correlation functions in this phase. The stripe patterns consist of a triangle array stripe and a uniform flat stripe. They can be reproduced respectively in the ladder model defined on the sites they occupy, in which the correlation in the stripe is short-ranged.

In previous meanfield studies of the SU(3) spin model on various lattices [32, 33], the lowest energy state is VCS. The stripe and chiral spin liquid phase is discovered for larger N . The VCS-stripe mixing state discovered here can be regarded as a step closer to the chiral spin liquid phase according to general phase diagram results [32, 68, 69]. Whether extra interaction can induct spin liquid requires further investigation.

Furthermore, under the 0th order approximation, the ground states of the model are local singlets on 3 of the vertices of one planar tetrahedron. These degenerate ground states can have different triangular configurations. The differ-

ent triangle patterns expand a configuration space as a quantum trimer model (Details in Supplemental Materials) [70]. An arrow representation could be constructed in accordance with the quantum dimer model study on Kagomé lattice [71]. Since each site is shared by two tetrahedrons and is associated with a singlet, we could define an arrow on one site that points toward the tetrahedron that the singlet belongs to. This arrow representation forms a restricted vertex model, whose mechanism may be related to the \mathbb{Z}_2 gauge theory[72].

VI. ACKNOWLEDGMENTS

This work was supported by the National Key Research and Development Program of China Grant No. 2022YFA1404204 and the National Natural Science Foundation of China (Grants No. 11625416 and No. 12274086). The authors acknowledge Fudan High Performance Computation Center for providing HPC resources that have contributed to the numerical results reported in this paper.

-
- [1] S. Stellmer, R. Grimm, and F. Schreck, Detection and manipulation of nuclear spin states in fermionic strontium, *Phys. Rev. A* **84**, 043611 (2011).
 - [2] S. Stellmer, M. K. Tey, B. Huang, R. Grimm, and F. Schreck, Bose-Einstein Condensation of Strontium, *Phys. Rev. Lett.* **103**, 200401 (2009).
 - [3] Y. N. M. de Escobar, P. G. Mickelson, M. Yan, B. J. DeSalvo, S. B. Nagel, and T. C. Killian, Bose-Einstein Condensation of ^{88}Sr , *Phys. Rev. Lett.* **103**, 200402 (2009).
 - [4] M. Kitagawa, K. Enomoto, K. Kasa, Y. Takahashi, R. Ciurylo, P. Naidon, and P. S. Julienne, Two-color photoassociation spectroscopy of ytterbium atoms and the precise determinations of s -wave scattering lengths, *Phys. Rev. A* **77**, 012719 (2008).
 - [5] M. Höfer, L. Riegger, F. Scazza, C. Hofrichter, D. Fernandes, M. Parish, J. Levinsen, I. Bloch, and S. Fölling, Observation of an Orbital Interaction-Induced Feshbach Resonance in ^{173}Yb , *Phys. Rev. Lett.* **115**, 265302 (2015).
 - [6] G. Pagano, M. Mancini, G. Cappellini, L. Livi, C. Sias, J. Catani, M. Inguscio, and L. Fallani, Strongly Interacting Gas of Two-Electron Fermions at an Orbital Feshbach Resonance, *Phys. Rev. Lett.* **115**, 265301 (2015).
 - [7] R. Zhang, Y. Cheng, H. Zhai, and P. Zhang, Orbital Feshbach Resonance in Alkali-Earth Atoms, *Phys. Rev. Lett.* **115**, 135301 (2015).
 - [8] M. A. Cazalilla, A. F. Ho, and M. Ueda, Ultracold gases of ytterbium: ferromagnetism and Mott states in an SU(6) Fermi system, *New J. Phys.* **11**, 103033 (2009).
 - [9] A. V. Gorshkov, M. Hermele, V. Gurarie, C. Xu, P. S. Julienne, J. Ye, P. Zoller, E. Demler, M. D. Lukin, and A. M. Rey, Two-orbital SU(N) magnetism with ultracold alkaline-earth atoms, *Nat. Phys.* **6**, 289 (2010).
 - [10] S. Taie, R. Yamazaki, S. Sugawa, and Y. Takahashi, An SU(6) Mott insulator of an atomic Fermi gas realized by large-spin Pomeranchuk cooling, *Nat. Phys.* **8**, 825 (2012).
 - [11] C. Hofrichter, L. Riegger, F. Scazza, M. Höfer, D. R. Fernandes, I. Bloch, and S. Fölling, Direct probing of the mott crossover in the SU(N) Fermi-Hubbard model, *Phys. Rev. X* **6**, 021030 (2016).
 - [12] H. Ozawa, S. Taie, Y. Takasu, and Y. Takahashi, Antiferromagnetic Spin Correlation of SU (N) Fermi Gas in an Optical Superlattice, *Phys. Rev. Lett.* **121**, 225303 (2018).
 - [13] D. Tusi, L. Franchi, L. F. Livi, K. Baumann, D. Benedicto Orenes, L. Del Re, R. E. Barfknecht, T.-W. Zhou, M. Inguscio, G. Cappellini, M. Capone, J. Catani, and L. Fallani, Flavour-selective localization in interacting lattice fermions, *Nat. Phys.* **18**, 1201 (2022).
 - [14] S. Taie, E. Ibarra-García-Padilla, N. Nishizawa, Y. Takasu, Y. Kuno, H.-T. Wei, R. T. Scalettar, K. R. A. Hazzard, and Y. Takahashi, Observation of antiferromagnetic correlations in an ultracold SU(N) Hubbard model, *Nat. Phys.* **18**, 1356 (2022).
 - [15] A. M. Müller, M. Lajkó, F. Schreck, F. Mila, and J. Minář, State selective cooling of SU (N) Fermi gases, *Phys. Rev. A* **104**, 013304 (2021).
 - [16] D. Yamamoto and K. Morita, Engineering of a Low-Entropy Quantum Simulator for Strongly Correlated Electrons Using Cold Atoms with SU(\mathcal{N})-Symmetric Interactions, *Phys. Rev. Lett.* **132**, 213401 (2024).
 - [17] C. Honerkamp and W. Hofstetter, Ultracold fermions and the SU(N) hubbard model, *Phys. Rev. Lett.* **92**, 170403 (2004).
 - [18] A. Sotnikov and W. Hofstetter, Magnetic ordering of three-component ultracold fermionic mixtures in optical lattices, *Phys. Rev. A* **89**, 063601 (2014).
 - [19] A. Sotnikov, Critical entropies and magnetic-phase-diagram analysis of ultracold three-component fermionic mixtures in optical lattices, *Phys. Rev. A* **92**, 023633 (2015).
 - [20] M. Hafez-Torbati and W. Hofstetter, Artificial SU(3) spin-orbit coupling and exotic Mott insulators, *Phys. Rev. B* **98**, 245131 (2018).
 - [21] G. Chen, K. R. Hazzard, A. M. Rey, and M. Hermele, Synthetic-gauge-field stabilization of the chiral-spin-liquid phase, *Phys. Rev. A* **93**, 245159 (2016).
 - [22] C. Feng, E. Ibarra-García-Padilla, K. R. A. Hazzard, R. Scalettar, S. Zhang, and E. Vitali, Metal-insulator transition and quantum magnetism in the SU(3) Fermi-Hubbard model, *Phys. Rev.*

- Res. **5**, 043267 (2023).
- [23] E. Ibarra-García-Padilla, C. Feng, G. Pasqualetti, S. Fölling, R. T. Scalettar, E. Khatami, and K. R. A. Hazzard, Metal-insulator transition and magnetism of SU(3) fermions in the square lattice, *Phys. Rev. A* **108**, 053312 (2023).
- [24] R. Assaraf, P. Azaria, M. Caffarel, and P. Lecheminant, Metal-insulator transition in the one-dimensional SU (N) Hubbard model, *Phys. Rev. B* **60**, 2299 (1999).
- [25] S. Capponi, P. Lecheminant, and K. Totsuka, Phases of one-dimensional SU(N) cold atomic Fermi gases-From molecular Luttinger liquids to topological phases, *Ann. Phys. (NY)* **367**, 50 (2016).
- [26] J.-C. He, J.-H. Zhang, J. Lou, and Y. Chen, Six-component pairing instability in the SU(4) t - J chain (2023), [arXiv:2311.06601](#).
- [27] H. Schlömer, F. Grusdt, U. Schollwöck, K. R. A. Hazzard, and A. Bohrdt, Subdimensional magnetic polarons in the one-hole doped SU(3) t - J model, *Phys. Rev. B* **110**, 125134 (2024).
- [28] J. Zhang, J. Hou, J. Lou, and Y. Chen, Ground state phase diagram of SU(3) t - J chain (2024), [arXiv:2409.09344](#).
- [29] M. Hermele and V. Gurarie, Topological liquids and valence cluster states in two-dimensional SU(N) magnets, *Phys. Rev. B* **84**, 245159 (2011).
- [30] A. Szasz, C. Wang, and Y.-C. He, Phase diagram of a bilinear-biquadratic spin-1 model on the triangular lattice from density matrix renormalization group simulations, *Phys. Rev. B* **106**, 115103 (2022).
- [31] R. Kaneko, S. Goto, and I. Danshita, Ground-state phase diagram of the SU(4) Heisenberg model on a plaquette lattice, *Phys. Rev. A* **110**, 023326 (2024).
- [32] X.-P. Yao, Y. Gao, and G. Chen, Topological chiral spin liquids and competing states in triangular lattice SU (N) Mott insulators, *Phys. Rev. Res.* **3**, 023138 (2021).
- [33] X.-P. Yao, R. L. Luo, and G. Chen, Intertwining SU (N) symmetry and frustration on a honeycomb lattice, *Phys. Rev. B* **105**, 024401 (2022).
- [34] J.-Y. Chen, J.-W. Li, P. Nataf, S. Capponi, M. Mambrini, K. Totsuka, H.-H. Tu, A. Weichselbaum, J. von Delft, and D. Poilblanc, Abelian SU(N)₁ chiral spin liquids on the square lattice, *Phys. Rev. B* **104**, 235104 (2021).
- [35] S. Niu, J.-W. Li, J.-Y. Chen, and D. Poilblanc, Chiral spin liquids with projected Gaussian fermionic entangled pair states, *Phys. Rev. B* **109**, L081107 (2024).
- [36] Y. Xu, S. Capponi, J.-Y. Chen, L. Vanderstraeten, J. Hasik, A. H. Nevidomskyy, M. Mambrini, K. Penc, and D. Poilblanc, Phase diagram of the chiral SU(3) antiferromagnet on the kagome lattice, *Phys. Rev. B* **108**, 195153 (2023).
- [37] T. A. Tóth, A. M. Läuchli, F. Mila, and K. Penc, Three-sublattice ordering of the SU(3) Heisenberg model of three-flavor fermions on the square and cubic lattices, *Phys. Rev. Lett.* **105**, 265301 (2010).
- [38] B. Bauer, P. Corboz, A. M. Läuchli, L. Messio, K. Penc, M. Troyer, and F. Mila, Three-sublattice order in the SU(3) Heisenberg model on the square and triangular lattice, *Phys. Rev. B* **85**, 125116 (2012).
- [39] A. Läuchli, F. Mila, and K. Penc, Quadrupolar Phases of the $S = 1$ Bilinear-Biquadratic Heisenberg Model on the Triangular Lattice, *Phys. Rev. Lett.* **97**, 087205 (2006).
- [40] A. Läuchli, F. Mila, and K. Penc, Erratum: Quadrupolar Phases of the $S = 1$ Bilinear-Biquadratic Heisenberg Model on the Triangular Lattice [Phys. Rev. Lett. 97, 087205 (2006)], *Phys. Rev. Lett.* **97**, 229901 (2006).
- [41] W.-J. Hu, S.-S. Gong, H.-H. Lai, Q. Si, and E. Dagotto, Density matrix renormalization group study of nematicity in two dimensions: Application to a spin-1 bilinear-biquadratic model on the square lattice, *Phys. Rev. B* **101**, 014421 (2020).
- [42] X.-T. Zhang, W.-J. Hu, E. Dagotto, and S. Gong, Fragility of the nematic spin liquid induced by diagonal couplings in the square-lattice SU(3) model, *Phys. Rev. B* **104**, 195135 (2021).
- [43] L. Herviou, S. Capponi, and P. Lecheminant, Even-odd effects in the J_1 - J_2 SU(n) heisenberg spin chain, *Phys. Rev. B* **107**, 205135 (2023).
- [44] T. Botzung and P. Nataf, Exact Diagonalization of SU(N) Fermi-Hubbard Models, *Phys. Rev. Lett.* **132**, 153001 (2024).
- [45] A. Weichselbaum, Qspace-an open-source tensor library for abelian and non-abelian symmetries (2024), [arXiv:2405.06632](#).
- [46] K. Sun, Z. Gu, H. Katsura, and S. Das Sarma, Nearly Flatbands with Nontrivial Topology, *Phys. Rev. Lett.* **106**, 236803 (2011).
- [47] T. Yoshioka, A. Koga, and N. Kawakami, Frustration effects in an anisotropic checkerboard lattice Hubbard model, *Phys. Rev. B* **78**, 165113 (2008).
- [48] S. Fujimoto, Geometrical-Frustration-Induced (Semi)Metal-to-Insulator Transition, *Phys. Rev. Lett.* **89**, 226402 (2002).
- [49] H. Katsura and A. Tanaka, Nagaoka states in the SU(n) Hubbard model, *Phys. Rev. A* **87**, 013617 (2013).
- [50] K. Tamura and H. Katsura, Ferromagnetism in the SU(n) Hubbard model with a nearly flat band, *Phys. Rev. B* **100**, 214423 (2019).
- [51] K. Tamura and H. Katsura, Ferromagnetism in d-Dimensional SU(n) Hubbard Models with Nearly Flat Bands, *J. Stat. Phys.* **182**, 16 (2021).
- [52] X. Hu, R.-W. Zhang, D.-S. Ma, Z. Cai, D. Geng, Z. Sun, Q. Zhao, J. Gao, P. Cheng, L. Chen, K. Wu, Y. Yao, and B. Feng, Realization of a Two-Dimensional Checkerboard Lattice in Monolayer Cu₂N, *Nano Lett.* **23**, 5610 (2023).
- [53] B. Canals, From the square lattice to the checkerboard lattice: Spin-wave and large- n limit analysis, *Phys. Rev. B* **65**, 184408 (2002).
- [54] J.-B. Fouet, M. Mambrini, P. Sindzingre, and C. Lhuillier, Planar pyrochlore: A valence-bond crystal, *Phys. Rev. B* **67**, 054411 (2003).
- [55] J.-S. Bernier, C.-H. Chung, Y. B. Kim, and S. Sachdev, Planar pyrochlore antiferromagnet: A large- N analysis, *Phys. Rev. B* **69**, 214427 (2004).
- [56] S. Chen, Y. Wang, W. Q. Ning, C. Wu, and H. Q. Lin, Exact ground state and elementary excitations of the spin tetrahedron chain, *Phys. Rev. B* **74**, 174424 (2006).
- [57] O. A. Starykh, A. Furusaki, and L. Balents, Anisotropic pyrochlores and the global phase diagram of the checkerboard antiferromagnet, *Phys. Rev. B* **72**, 094416 (2005).
- [58] R. F. Bishop, P. H. Y. Li, D. J. J. Farnell, J. Richter, and C. E. Campbell, Frustrated Heisenberg antiferromagnet on the checkerboard lattice: J_1 - J_2 model, *Phys. Rev. B* **85**, 205122 (2012).
- [59] P. H. Y. Li and R. F. Bishop, Ground-state phase structure of the spin- anisotropic planar pyrochlore, *J. Phys.: Condens. Matter* **27**, 386002 (2015).
- [60] S. Capponi, Numerical study of magnetization plateaus in the spin- $\frac{1}{2}$ Heisenberg antiferromagnet on the checkerboard lattice, *Phys. Rev. B* **95**, 014420 (2017).
- [61] J. Wildeboer, Z. Nussinov, and A. Seidel, Exact solution and correlations of a dimer model on the checkerboard lattice, *Phys. Rev. B* **102**, 020401 (2020).
- [62] P. Corboz, K. Penc, F. Mila, and A. M. Läuchli, Simplex solids in SU(N) Heisenberg models on the kagome and checkerboard lattices, *Phys. Rev. B* **86**, 041106 (2012).
- [63] L. Balents, Spin liquids in frustrated magnets, *Nature* **464**, 199 (2010).

- [64] C. Lacroix, P. Mendels, and F. Mila, eds., *Introduction to Frustrated Magnetism: Materials, Experiments, Theory*, Springer Series in Solid-State Sciences, Vol. 164 (Springer, 2011).
- [65] P. Weinberg and M. Bukov, QuSpin: a Python package for dynamics and exact diagonalisation of quantum many body systems part I: spin chains, *SciPost Phys.* **2**, 003 (2017).
- [66] P. Weinberg and M. Bukov, QuSpin: a Python package for dynamics and exact diagonalisation of quantum many body systems. Part II: bosons, fermions and higher spins, *SciPost Phys.* **7**, 020 (2019).
- [67] M. Fishman, S. R. White, and E. M. Stoudenmire, The ITensor Software Library for Tensor Network Calculations, *SciPost Phys. Codebases*, **4** (2022).
- [68] M. Hermele, V. Gurarie, and A. M. Rey, Mott Insulators of Ultracold Fermionic Alkaline Earth Atoms: Underconstrained Magnetism and Chiral Spin Liquid, *Phys. Rev. Lett.* **103**, 135301 (2009).
- [69] C. Boos, C. J. Ganahl, M. Lajkó, P. Nataf, A. M. Läuchli, K. Penc, K. P. Schmidt, and F. Mila, Time-reversal symmetry breaking Abelian chiral spin liquid in Mott phases of three-component fermions on the triangular lattice, *Phys. Rev. Res.* **2**, 023098 (2020).
- [70] S. Jandura, M. Iqbal, and N. Schuch, Quantum trimer models and topological SU(3) spin liquids on the kagome lattice, *Phys. Rev. Res.* **2**, 033382 (2020).
- [71] G. Misguich, D. Serban, and V. Pasquier, Quantum Dimer Model on the Kagome Lattice: Solvable Dimer-Liquid and Ising Gauge Theory, *Phys. Rev. Lett.* **89**, 137202 (2002).
- [72] H. Yan and R. Pohle, Classical \mathbb{Z}_2 spin liquid on the generalized four-color kitaev model (2024), [arXiv:2409.04061](https://arxiv.org/abs/2409.04061).

Supplemental Materials for “Bond Stripe Patterns in SU (3) spin model on checkerboard lattice”

S1. DMRG SIMULATION IN SQUARE FRAME

The interaction we tune turns the lattice from a square one to a planar pyrochlore. The ground state patterns in square frame direction are calculated as a reference to verify the existence of the possible order. 3-sublattice antiferromagnetic order are obviously suppressed from the very short penetration depth of the spin polarization (FIG. S1(a)). We also try to induce valence bond order by some stronger interaction near the boundary (FIG. S1(b) – (d)). The inhomogeneity of bond just extend to as far as several unitcells, with staggered bonds induced by open boundary on x direction remaining.

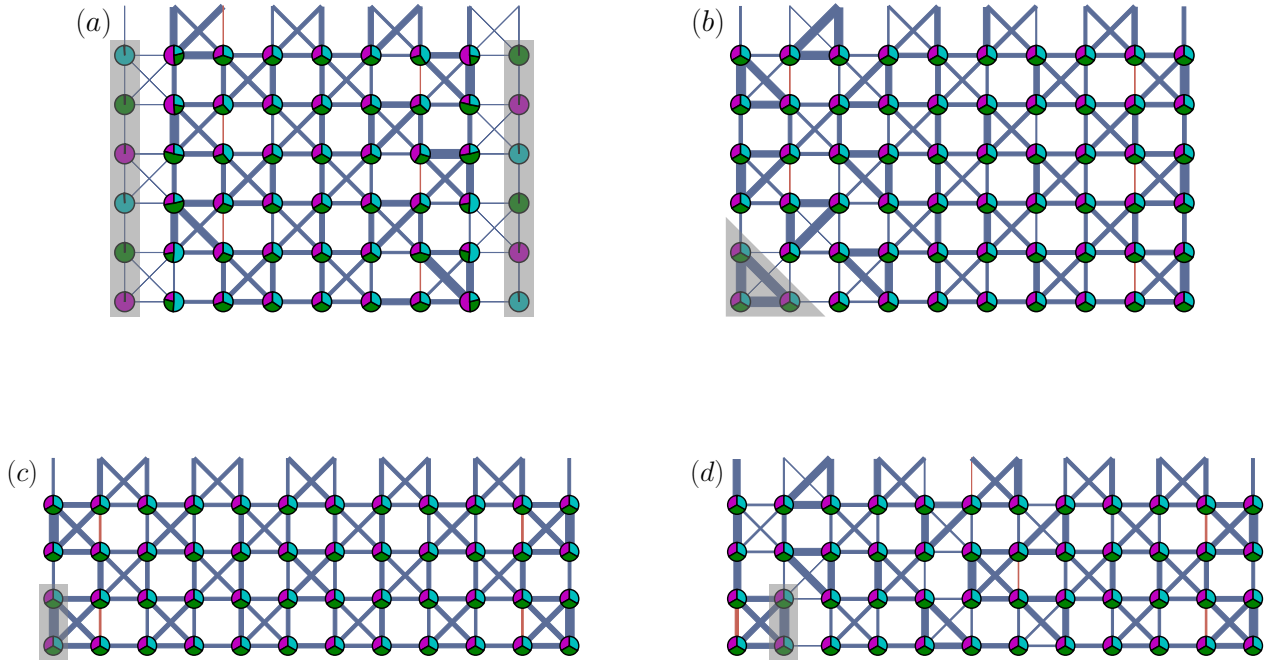


FIG. S1: Bond energies and local color densities on square lattice with different inducing structure on boundary (gray-covered region). Open boundary condition on x direction and periodic boundary condition on y direction. (a) External fields inducing antiferromagnetic order applied on the boundary sites; (b) Stronger interaction on bonds in a triangle; (c) Stronger interaction on a single bond; (d) Stronger interaction on a single bond whose correlation is weak in previous results.

S2. DMRG SIMULATION OF DIFFERENT SIZES

Bond energies and local color densities are presented for different sizes of the system by DMRG calculations. We extend the $(7, 4)$ system to $(10, 4)$, which keeps the total number of spins a multiple of 3, and plot the real space patterns of the lowest energy state and some competing states in FIG. S2.

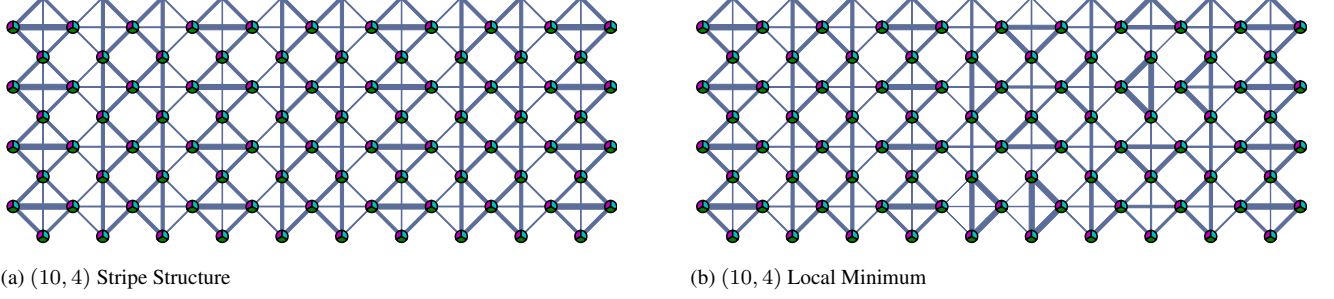


FIG. S2: Ground state (S2a) and local minimum state (S2b) real-space bond strength obtained by DMRG simulation for the system size of $(10, 4)$. The energy of the states are (S2a) $E_0 = -286.548$, (S2b) $E_1 = -286.283$. Their pattern could be regarded as patterns of 7×4 low energy states with an extra stripe period.

Then we extend the size in y direction to $(7, 5)$ and $(7, 6)$. The results are shown in FIG. S3.

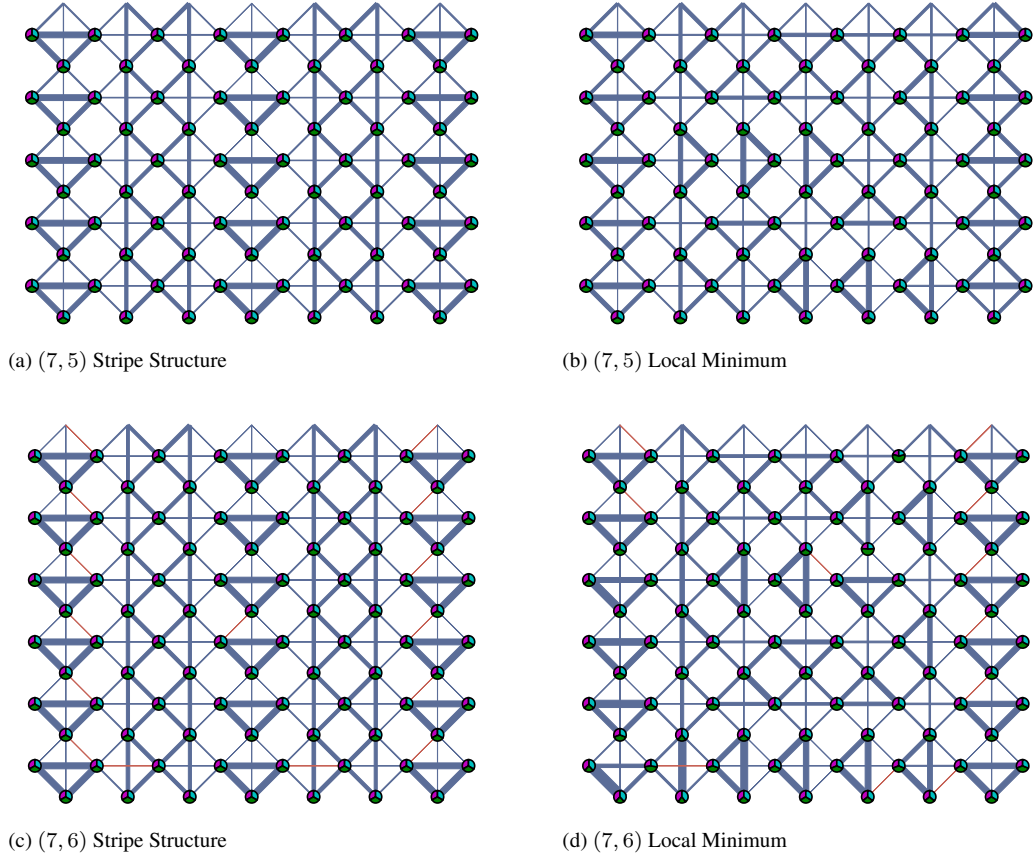


FIG. S3: Ground state (S3a, S3c) and local minimum state (S3b, S3d) real-space bond strength obtained by DMRG simulation for the system size of $(7, 5)$ and $(7, 6)$. The energy of the states is (S3a) $E_0 = -250.928$, (S3b) $E_0 = -250.520$, (S3c) $E_0 = -300.598$, (S3d) $E_0 = -299.661$. The energy of bond stripe states is lower.

When the size in the y direction is 6, we can freely set up the size in x direction with the total spin number a multiple of 3. The results are shown in FIG. S4.

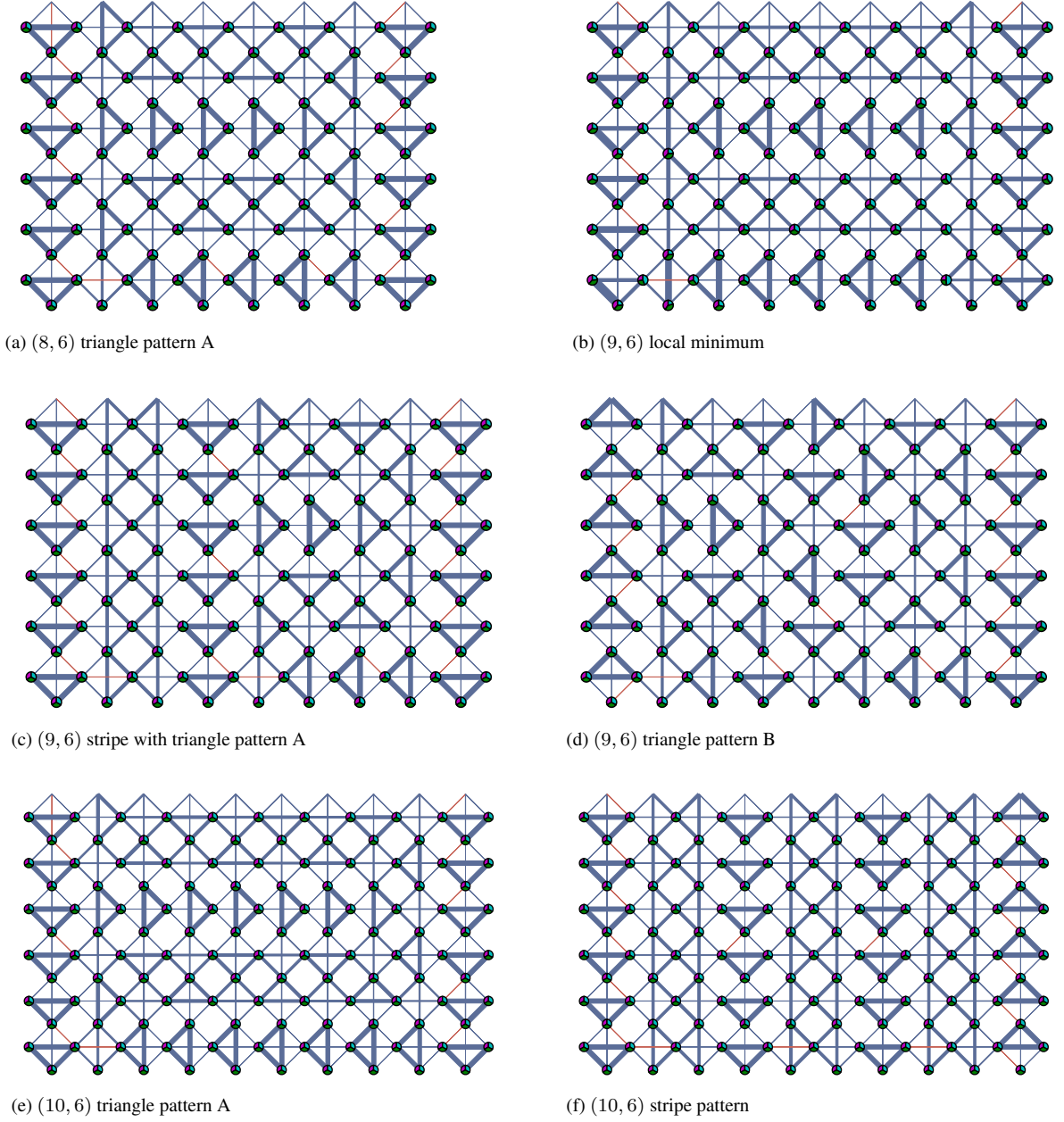


FIG. S4: Ground states and local minimum states obtained by DMRG simulation for the system width $N_y = 6$. The energy of the states are (S4a) $E_0 = -342.361$, (S4b) $E_0 = -384.193$, (S4c) $E_0 = -384.550$, (S4d) $E_0 = -384.070$, (S4e) $E_0 = -426.819$, (S4f) $E_0 = -426.903$. The bond stripe states have better energy.

S3. LOW ENERGY EFFECTIVE THEORY OF LOCAL TRIANGLE SINGLET

The arrow mapping rule is shown in FIG. S5 and a real space example is shown in FIG. S6.

Through the mapping, the local triangle singlet pattern in the low energy effective theory corresponds to a restricted vertex model space. This vertex model space has only sources and no sinks. The flow of arrows is not constant, but it enters into a loop. In the previous finite size DMRG calculation, we can find that the boundary configurations are loop structures.

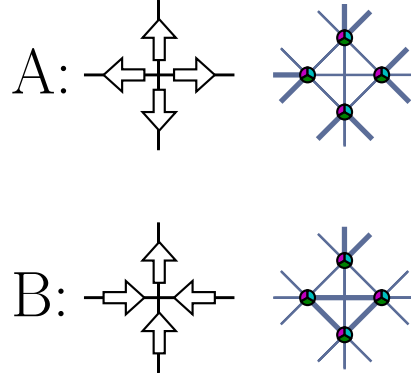


FIG. S5: Mapping for the local triangle singlet to the arrow representation: case A represents four spins in the unit cell form a 3-spin singlet in its surrounding unit cell; case B represents three spins in the unit cell form a $SU(3)$ singlet, and one spin forms singlet in the adjacent unit cell.

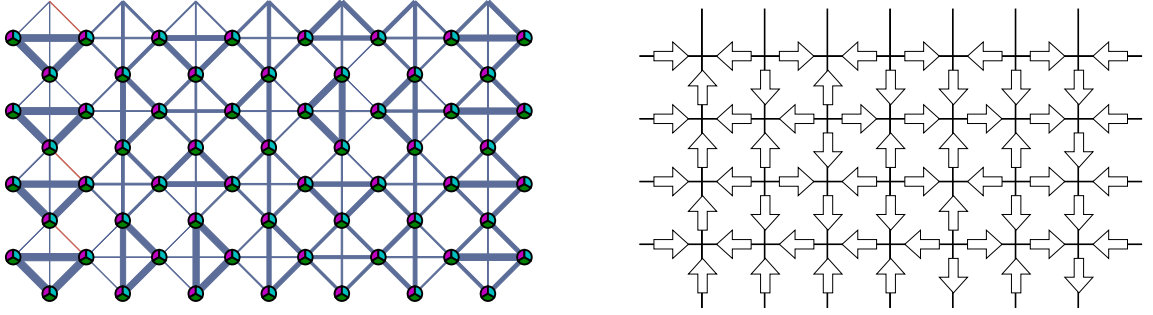


FIG. S6: An example of the local triangle singlet for the system size $(4, 7)$ and its arrow representation.

As shown in FIG. S7, for the system size $(N_x, N_y) = (9, 6)$, there are two inner structures. They are both divided by an in-body loop structure.

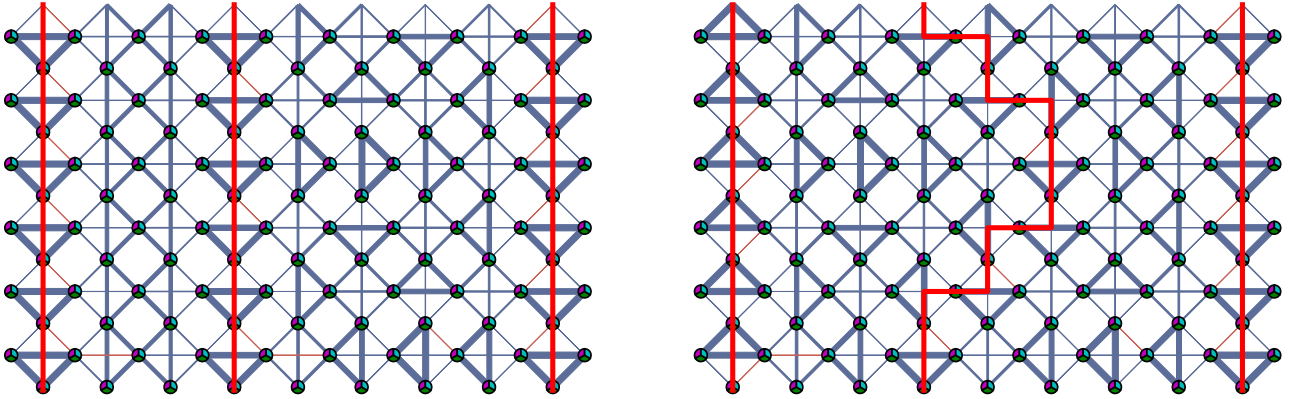


FIG. S7: Two loop structures for the system size $(N_x, N_y) = (9, 6)$, labeled by red lines. Obviously, the reverse operation on the arrows also corresponds to a real space configuration.